Available online at www.sciencedirect.com

ScienceDirect

Journal of Solid State Chemistry 179 (2006) 3478–3483

JOURNAL OF SOLID STATE CHEMISTRY

www.elsevier.com/locate/jssc

Defect microstructures of TiO_2 rutile due to Zr^{4+} dissolution and expulsion

K.C. Yang, P. Shen*, D. Gan

Institute of Materials Science and Engineering, National Sun Yat-sen University, Kaohsiung, Taiwan, ROC

Received 23 April 2006; received in revised form 12 July 2006; accepted 16 July 2006
Available online 20 July 2006

Abstract

Defect microstructure of Zr-dissolved TiO_2 polycrystals, homogenized as rutile structure at 1600 °C and then aged at 900 °C for 2–200 h in air, was characterized by analytical electron microscopy. Diffuse diffractions occurred at 1/2(211) as a result of Zr^{4+} substitution for Ti^{4+} with volume/charge compensating defect clusters. Upon annealing at 900 °C, plate-like Guinier and Preston (G.P.) zone appeared with the plate surface parallel to (100) and (010) and in association with dislocations. Commensurate superstructures with apparent triple {101} and {111} periodicity also occurred as metastable intermediates, which are presumably the precursor of the equilibrium $ZrTi_2O_6$ precipitate.

Keywords: TiO_2; Rutile; Zr dopant; Defect clusters; TEM

1. Introduction

Transition metal monoxides of rock salt type structure, which show considerable extent of nonstoichiometry due to dopant, commonly form defect clusters of paracrystalline distribution as the precursor of spinel oxide precipitate [1–5]. (The paracrystalline distribution is such that the spacing between defects remains fairly constant but the relative lateral translation is variable [6].) Paracrystal also occurs in the spinel precipitates by oxidation and/or doping [7–9]. Alternatively, Guinier and Preston (G.P.) zones may appear and act as a metastable intermediate for the spinel precipitate when a large extent of composition change is required for the precipitation process, such as the precipitation of Mg_2TiO_4 compound spinel upon exsolution of Ti-dissolved MgO [9]. (Copper-rich zones in Al–Cu alloys were detected in 1938 by G.P. from streaks in X-ray diffraction patterns. In fact, G.P. never met, though the zones were ever after known as Guinier–Preston zones [10].)

Zr-doped rutile is of interest due to the possibility of chemical stabilization of a high-pressure phase [11], in particular the α-PbO_2-type TiO_2 (space group *Pbcn*), which exists as nanometer-size inclusion in garnet of ultrahigh-pressure metamorphic rock [12]. This high-pressure polymorph of rutile, appearing under pressure above several GPa depending on the particle size and temperature, can be synthesized by shock or static compression, as overviewed recently [13]. On the other hand, coherency strain and possible nano-size effect during the precipitation process caused the precipitation of α-PbO_2-type TiO_2 in sapphire (Ti-doped Al_2O_3) as an intermediate phase at ambient pressure [14]. The distorted α-PbO_2-type precipitates then transformed to needle-like rutile by the loss of coherency with respect to sapphire and the phase transformation was suggested to be purely structural in nature [15]. As for the chemical stabilization effect, it was reported that the substitution of Ti^{4+} with Zr^{4+} causes the stabilization of $ZrTiO_4$ as the high-pressure α-PbO_2-type isostructure at ambient pressure [16].

The motivation of this research is to study the precipitation of metastable phases in Zr^{4+} dissolved TiO_2 rutile, and to compare the results with well-documented defect clustering in cation-doped transition metal

---

*Corresponding author. Fax: +1 886 7 5254099.
E-mail address: pshen@mail.nsysu.edu.tw (P. Shen).

0022-4596/$ - see front matter
doi:10.1016/j.jssc.2006.07.020

monoxides. Detailed analytical electron microscopic (AEM) observations were made on the Zr-dissolved TiO_2 polycrystals, which was annealed in the two-phase stable-phase field of $ZrTi_2O_6$ (space group *Pbcn*) and TiO_2 [16]. Rather than paracrystal or α-PbO_2-type structure, G.P. zones and commensurate planar defects in association with dislocations, were formed as metastable intermediate. The combined effects of oversaturation, undercooling and defect chemistry/microstructure on the metastable precipitates are addressed, as well as the potential catalytic applications of Zr-doped TiO_2.

2. Experimental procedures

TiO_2 powders (Aldrich, 99.9%) mixed with 8 mol% ZrO_2 (Cerac, 99.9%) were dry-pressed at 650 MPa into disks 10 mm in diameter and 2 mm in thickness, and then reactively sintered at 1600 °C for 24 h in air, followed by furnace cooling to room temperature. The sintered specimens were further aged at 900 °C for 2–200 h in air and then air quenched to room temperature.

The fired specimens were analyzed by X-ray diffraction (XRD, Cu*K*α, 40 kV, 30 mA, using Siemens D5000 diffractometer) at a scanning rate of 1°/min (step size 0.05°, fixed counts 3 s) to identify the crystalline phases. The *d*-spacings measured from XRD traces were used for least-squares refinement of the lattice parameters within ±0.0003 nm.

The sintered specimen was polished for scanning electron microscopic (SEM, JEOL JSM-6400, 20 kV) observations. Back-scattered electron image (BEI) was used to characterize the grain size and the composition distribution.

Thin sections of the fired samples were Ar-ion milled to electron transparency and observed with AEM (JEOL3010, 300 kV) coupled with energy dispersive X-ray (EDX) analysis. The L shell counts of Zr and K shell counts of Ti without absorption correction were used for the semi-quantitative determination of composition at the scale of individual grains. Bright field image (BFI) and dark field image (DFI) taken by transmission electron microscopy (TEM) were used to study the morphologies of the defects. Selected area electron diffraction (SAED) pattern and lattice image coupled with two-dimensional (2-D) Fourier transform and inverse transform were used to analyze the crystal structure and defects of the Zr-dissolved rutile.

3. Results

3.1. XRD and SEM

The samples reactively sintered at 1600 °C for 24 h or further aged at 900 °C for 2–200 h show only Zr-dissolved rutile in XRD traces (Fig. 1), although minor precipitates were observed by TEM. The peak intensities of the Zr-dissolved rutile vary among samples because of the grain size can be as large as 100 μm after sintering, as revealed by SEM micrograph in Fig. 2. The as-sintered samples were used for XRD because the sintered TiO_2–ZrO_2 are hard and difficult, if not impossible, to grind. Besides, grinding may introduce residual stress and even phase transformations, which would interfere with the aging effect on defects and phase transformations that we focused on.

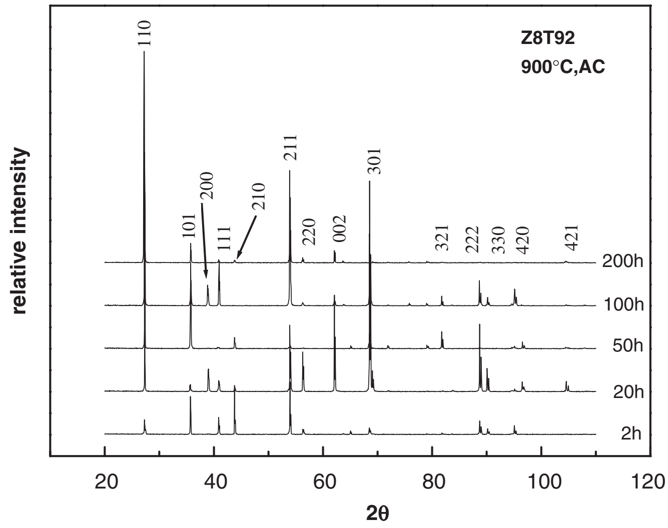

Fig. 1. XRD traces of Zr-dissolved rutile in samples homogenized at 1600 °C for 24 h followed by aging at 900 °C for 2–200 h showing that only rutile is present, although the intensities of diffraction peaks varied considerably due to large grain size. The traces were compiled by lowering the background without losing the peaks for a comparison.

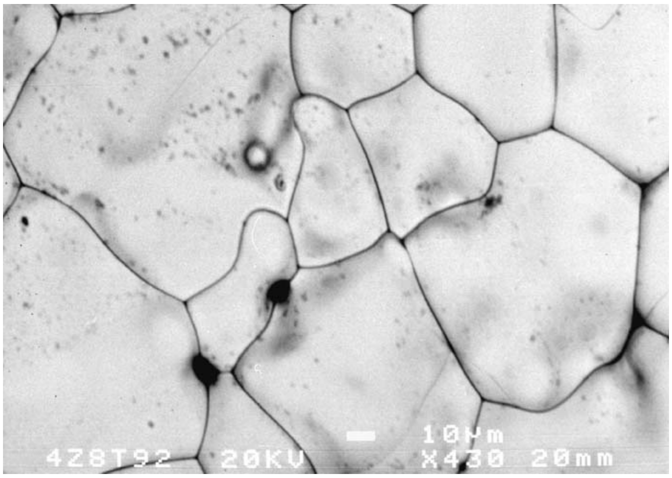

Fig. 2. SEM BEI showing the Zr-dissolved rutile reactively sintered at 1600 °C for 24 h has grains up to 100 μm in size with occasional pores at grain boundaries.

The least-squares refinement of the *d*-spacing indicated the as-sintered Zr-dissolved rutile has room temperature lattice parameters of $\mathbf{a} = 0.4616 \pm 0.0003$ and $\mathbf{c} = 0.2988 \pm 0.0003$ nm, which are significantly larger than those of the undoped rutile ($\mathbf{a} = 0.4593$ nm and $\mathbf{c} = 0.2959$ nm, JCPDS file 21–1276). Further annealing at 900 °C for 2–200 h did not cause any appreciable change in the lattice parameters despite the induced defect clustering and metastable precipitates. In general, superlattice reflections are from minor phase of the sintered specimens and therefore hardly detected by XRD, but can be readily observed by TEM.

3.2. TEM

TEM BFI shows no precipitates in the Zr-doped rutile reactively sintered at 1600 °C for 24 h (not shown). Corresponding SAED pattern shows diffuse diffraction at the $G \pm 1/2(\bar{2}\bar{1}1)^*$ regions of reciprocal space with streaks parallel to [001] of rutile (Fig. 3). It is not clear if such diffuse superlattice diffractions can be attributed to the incipient development of defect clusters and/or disordering/ordering upon furnace cooling analogous to the phase behavior of other dioxides such as fully stabilized zirconia with charge/volume compensating defect clusters as well documented in the literature [17,18]. After aging at 900 °C for 2 h, dislocation arrays, but without any associated precipitates were observed (Fig. 4). The tangled dislocations as indicated by arrows in Fig. 4a were unambiguously identified by weak beam analysis (not shown).

The Zr-dissolved rutile subject to prolonged aging at 900 °C for 200 h followed by air quenching showed G.P. zone-like thin plate precipitates. Fig. 5a shows that there are two variants parallel to the rutile (100) and (010) planes as viewed along the *c* axis ($Z = [001]$), which caused spots splitting along [100] and [010] directions, respectively (Fig. 5b). Lattice image (Fig. 5c) and reconstructed image (Fig. 5d) from the 2-D Fourier transform of Fig. 5c further showed the semicoherent nature of the precipitates and the dislocation half planes parallel to $(\bar{1}10)$ and (110). It is difficult, if not impossible, to tilt wide angles of the TEM specimen in order to tell whether the G.P.-zone like thin plate precipitates, which appeared edge-on only in [001] zone axis, are in all grains or only in some.

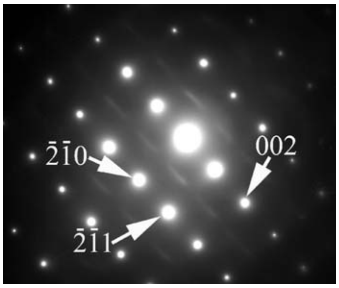

Fig. 3. TEM SAED pattern in $[\bar{1}20]$ zone axis showing diffuse superlattice diffractions $\sim\frac{1}{2}(\bar{2}\bar{1}1)$ with streaking along the *c*-axis. The Zr-doped rutile sample was reaction-sintered at 1600 °C for 24 h.

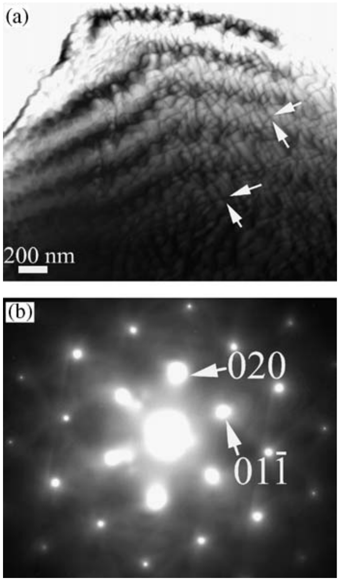

Fig. 4. TEM (a) BFI and (b) SAED pattern in [100] zone axis showing dislocation arrays indicated by arrows. Sample reactively sintered at 1600 °C for 24 h and aged at 900 °C for 2 h.

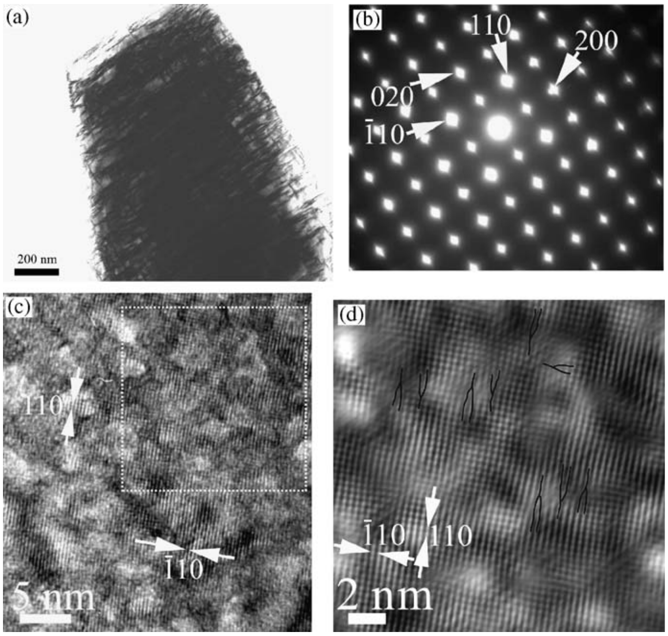

Fig. 5. (a) TEM BFI viewed along *c*-axis showing two variants of plate-like precipitates. (b) SAED pattern in [001] zone axis showing diffraction spot splitting along [100] and [010] directions. (c) Lattice image of G.P. zone-like domains. (d) Reconstructed image from the square region in (c) showing G.P. zone variants and dislocations with $(\bar{1}10)$ and (110) half planes, as delineated by dark lines. Sample homogenized at 1600 °C for 24 h and aged at 900 °C for 200 h.

The same specimen as Fig. 5 showed commensurate superstructures when viewed perpendicular to the [001] axis (Figs. 6–8). Fig. 6 shows that the SAED pattern in [100] zone axis carries apparent superlattice spots at $1/3(0\bar{1}1)$ and $1/3(0\bar{1}\bar{1})$. Complicated transient phases co-exist and appear to vary at the scale of individual grains in the sample. Besides the G.P. zones and the epitaxial hematite structure as indicated by the 2/3{011} superlattice spots, analogous to those of Fe-bearing precipitates in metamorphic rutile [19] as addressed later, there are defect clusters more or less extended to give 1/2(211) superstructure diffractions. (cf. Figs. 4 and 12 of Ref. [19] for the 1/3{101} and 2/3{101} diffractions of rutile, which are, respectively, the dynamic diffractions and the allowed

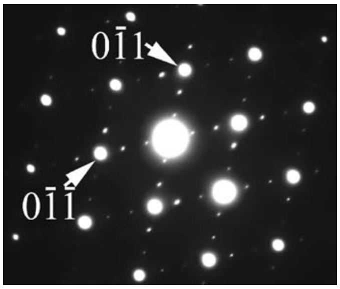

Fig. 6. SAED pattern in [100] zone axis showing apparent superlattice spots 1/3(0$\bar{1}$1) and 1/3(0$\bar{1}\bar{1}$). The specimen is the same as Fig. 5.

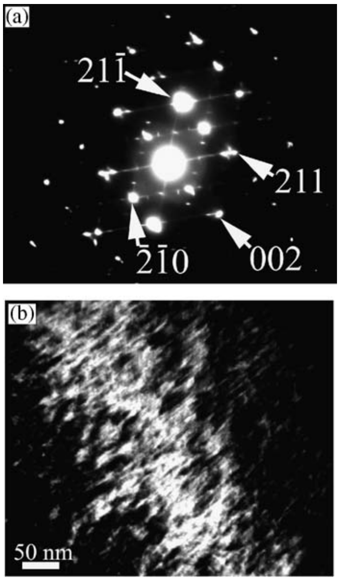

Fig. 7. (a) SAED pattern in [$\bar{1}$20] zone axis showing apparent 1/2(211) superstructure diffraction, the streaks along reciprocal plane normal directions (211)* and (21$\bar{1}$)*, and the side band associated with each diffraction spot, including (001) and its multiple. (b) DFI ($g = \bar{2}\bar{1}0$) showing planar modulation contrast parallel to (001). The specimen is the same as Fig. 5.

diffractions of hematite.) In the [$\bar{1}$20] zone axis, the Zr-dissolved rutile shows 1/2(211) superstructure diffractions with streaks along reciprocal plane normal directions (211)* and (21$\bar{1}$)*, and side band diffractions associated with fundamental diffractions (Fig. 7a). The diffuse diffraction is part of a more extended continuous diffuse distribution in the sample without aging (Fig. 3), but appears to be genuinely centered on the $G \pm 1/2(\bar{2}\bar{1}1)^*$ regions of reciprocal space after aging at 900 °C (Fig. 7). DFI shows planar modulated contrast parallel to the (001) plane (Fig. 7b). In the [110] zone axis, the Zr-dissolved rutile shows apparent 1/3(1$\bar{1}\bar{1}$) superlattice spot and the (110) spot degenerated into cross-like side bands (Fig. 8a). In fact, the cross-like side bands are associated with all reflections except for *hkl* (*h*, *k* and *l* are all even or all odd. DFI formed with $\bar{1}$10 spot and side bands indicated that they were diffracted from nanometer-size defect clusters (Fig. 8b). It should be noted that the rutile has a space group of $P4_2$/mnm (No. 136) having 0 0 1 and 0 0 1 diffractions forbidden. (According to International Tables for Crystallography, the general reflection conditions of this space group are $0kl$: $k+l=2n$; $00l$: $l=2n$; $h00$: $h=2n$.) Such reflections may appear as double diffractions in some zone axes (Figs. 3, 7a and 8a) but not others (Figs. 4b and 6) depending on the allowed other diffractions in the zone axis.

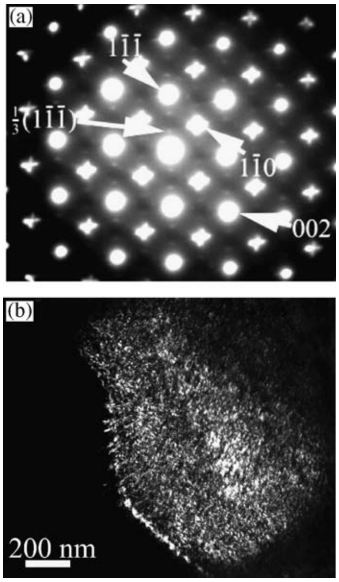

Fig. 8. (a) SAED pattern in [110] zone axis showing apparent 1/3(1$\bar{1}\bar{1}$) superlattice spot and cross-like side-bands associated with (110) diffraction. (b) DFI ($g = \bar{1}10$) showing the nanometer-size domains of defect clusters. The specimen is the same as Fig. 5.

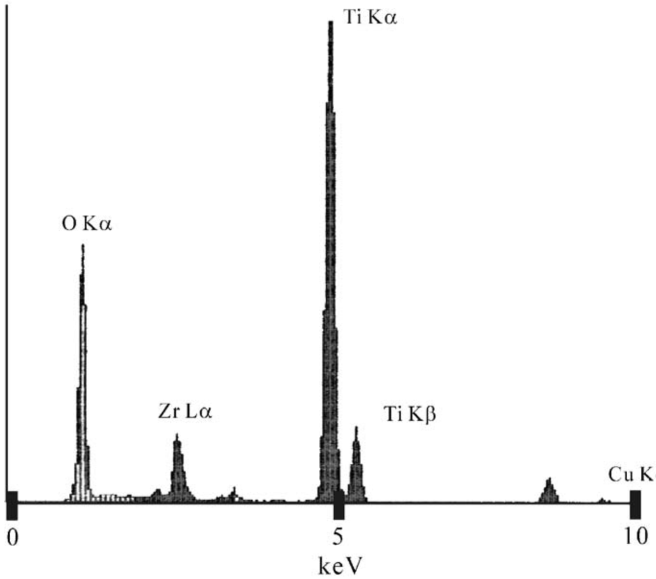

Fig. 9. Point-count EDX spectrum of Zr-doped rutile showing counts of Ti, O, and Zr. (The Cu count comes from the specimen holder.) The specimen is the same as Fig. 5.

Point-count EDX spectrum in Fig. 9 shows the Zr content is as high as 9 at% for Zr-dissolved rutile. The superlattice and defect cluster domains are not large enough for the composition difference to be measured.

4. Discussion

4.1. Solid solubility of ZrO_2 in rutile

According to Ref. [20], the solid solubility of Zr in titania decreases with decreasing temperature, from about 18 mol% at 1760 °C to 12% at 1370 °C, and to 6% at 980 °C. The solid solubility of ZrO_2 in rutile is less than 8 mol% at 900 °C. At this aging temperature, a bulk composition of 8 mol% ZrO_2 falls in the two-phase region of $ZrTi_2O_6$ (space group *Pbcn*) and TiO_2 [19]. Due to the combined effects of oversaturation and undercooling, Zr^{4+} was expelled from the rutile host to form specific metastable precipitates in the present study as addressed in Section 4.4.

4.2. Thermal and surface effects on the Ti^{3+}/Ti^{4+} ratio

TiO_{2-x} was one of the typical oxygen-deficient oxides [21] and many studies of rutile have been reported [22,23]. The nonstoichiometry in this oxide can be explained as a series of ordered phases (Magnéli phases) following a common formula such as Ti_nO_{2n-1}. This nonstoichiometric rutile is an *n*-type semiconductor in which the dominant defects are titanium interstitials and/or oxygen vacancies.

Generation of electrons in the TiO_{2-x} lattice may proceed through the following equations in Kröger–Vink notation [24]:

$$TiO_2 \rightarrow Ti_i^{\bullet\bullet\bullet\bullet} + 4e' + O_2,$$

$$TiO_2 \rightarrow Ti_i^{\bullet\bullet\bullet} + 3e' + O_2,$$

$$\tfrac{1}{2}TiO_2 \rightarrow V_O^{\bullet\bullet} + 2e' + \tfrac{1}{2}O_2.$$

A defect reaction can be written for each of the three modes of reduction involving the point defects Ti_i^{4+} or Ti_i^{3+} interstitials or O^{2-} vacancies [25]. Kofstad and Hed [26] suggested that $V_O^{\bullet\bullet}$ predominates at high oxygen partial pressure and low temperature, whereas $Ti_i^{\bullet\bullet\bullet}$ and $Ti_i^{\bullet\bullet\bullet\bullet}$ are dominant at high temperature and low oxygen partial pressure. Also, from the measured slope of the logarithm plot of Ti diffusion coefficient versus oxygen partial pressure, it was concluded that Ti_i^{3+} contributes more at lower temperature.

Metal vacancy concentration can be higher near the grain boundary or free surface than in the bulk. For example, the nickel vacancy increases by a factor of about 40 over the bulk value for the (211)/[011] twist grain boundary of $Ni_{1-x}O$ at 727 °C [27]. The near-surface layers of Fe_2O_3 [28] and CoO [29] also have much larger deviations from stoichiometry and higher defect concentrations than the bulk.

It is not clear if TiO_{2-x} has specific type of defect prevailing near the grain boundary and free surface at high temperature and the oxygen partial pressure of air. In any case, the Zr^{4+} substitution for Ti^{4+} has significant effect on the defect clustering and/or ordering in the present sample, as shown in the following discussion.

4.3. Zr^{4+} induced defect clusters

Comparing with the undoped rutile, the increased lattice parameter of the Zr-dissolved rutile is consistent with the substitution of Zr^{4+} (0.072 nm) for Ti^{4+} (0.061 nm), both radii are effective in coordination number (CN) of 6 [30]. The inclusions of larger cations at high temperature caused large internal stress and plastic deformation of the rutile crystal, as manifested by the dislocation arrays in Fig. 4. The incorporation of larger cations could also induce $V_O^{\bullet\bullet}$ for volume compensation, which could induce Ti'_{Ti} for charge compensation. It is not known whether defect clusters such as $[Ti'_{Ti} - V_O^{\bullet} - Ti'_{Ti}]$ could form from oxygen vacancy. It is apparent, however, that paracrystal with 4:1 type defect clusters does not occur in the present rutile with oxygen deficiency. By contrast, in oxides of rock salt structure with cation vacancies, 4:1 clusters are formed and arranged as paracrystal [1–8].

There is a larger cell volume of Zr-doped rutile than undoped rutile due to the substitution of Zr^{4+} with smaller-size Ti^{4+} in CN 6 as mentioned. Based on the lattice parameters determined by XRD, the molar volume of rutile increases by 2% for the present sample with 8 mol% ZrO_2 in dissolution. It is however beyond the scope of this study to tell whether there is any deviation of lattice parameter/molar volume relations from Vegard rule due to specific defect clusters.

4.4. Metastable exsolution

Side-band diffractions of aged Zr-dissolved rutile appeared to come from nanometer-size domains of defect clusters (Fig. 8b). In this regard, defect clustering by atom redistribution process can account for the diffuse scattering effects in the electron diffraction patterns, as suggested by Khachaturyan [31] in the case of iron–carbon martensite in which the diffuse intensity is resulted from carbon redistribution. The effect may even approach to the extent of spinodal decomposition [31], in the early stage of which the amplitudes of all concentration waves with wave vectors in the instability range increase exponentially with time. The region around each fundamental spot of reciprocal lattice gives the shape of diffuse scattering intensity maxima, which are associated with concentration heterogeneities produced by spinodal decomposition.

Apparently, G.P. zone and commensurate superstructures are metastable precipitates and may possibly be the precursor of $ZrTi_2O_6$, whose formation requires a long dwelling time at rather low temperature due to the sluggish diffusion kinetics. In this regard, the structure of rutile has edge-sharing octahedral chains and therefore open channels along the *c*-axis [10]. These open channels allow fast diffusion of the small (interstitial) divalent impurity cations but only slow diffusion of the substitutional Ti^{4+} and Zr^{4+} [32]. Still, the exsolution of metastable plate-like G.P. zone and commensurate superstructures from Zr-dissolved rutile may take advantage of the relatively weak linkage of $\{100\}$, {110}, and (210) planes in the [001] zone axis due to the volume compensating oxygen vacancies. The apparent tripling of the {101} and {111} spacings (Figs. 6 and 8) may be due to corundum-like structure in view of the fact that the Fe-bearing twin platelets in metamorphic rutile have been identified to be of the corundum isostructure of hematite (or Ti_2O_3) [19]. (These twin platelets are coherently intergrown parallel to (100) and (010) of metamorphic rutile and the dynamic diffraction effect induces the apparent tripling of the {101} spacings [19].) In fact, the SAED pattern in Fig. 6 can be interpreted as the hematite-type twin variants (denoted as *h*) superimposed with the rutile (denoted as *r*) following the crystallographic relationship $[0001]_h \| [100]_r$; $\langle 10\bar{1}0\rangle_h \| [010]_r$ as indexed in Fig. 12c of Ref. [19].

Finally, it should be noted that ordering to form commensurate or incommensurate superstructure might proceed simultaneously with defect clustering in the present Zr-dissolved rutile upon aging at 900 °C. In this connection, recent theoretical calculations considering the interactions with the second nearest neighbors in addition to the first ones indicated that defect clustering and ordering may both be valid diffusional pathways in the decomposition of alloys [33].

5. Conclusions

Zr-dissolved TiO_2 polycrystals reactively sintered at 1600 °C showed diffuse diffractions due to the defect clusters formed with volume/charge compensating defects as a result of the Zr^{4+} substitution for Ti^{4+}.

It was suggested that the oxygen vacancy is the dominant type of defects and the $[Ti'_{Ti} - V_O^{\bullet\bullet} - Ti'_{Ti}]$ type defect clusters rather than paracrystals may be formed in Zr-doped rutile.

Owing to the sluggish diffusion kinetics at the aging temperature of 900 °C, metastable G.P. zone, and commensurate superstructures precipitated in Zr-doped rutile, possibly as precursors of the equilibrium $ZrTi_2O_6$.

Acknowledgments

We thank L.J. Wang for technical assistance on AEM and anonymous reviewers for constructive comments. This work was supported by the Center for Nanoscience and Nanotechnology at NSYSU and National Science Council, Taiwan, ROC under contract NSC94-2216-E119-005.

References

[1] P. Shen, S. Chen, H.S. Liu, Mater. Sci. Eng. A 161 (1993) 135–143.
[2] J. Chen, P. Shen, J. Solid State Chem. 140 (1998) 361–370.
[3] K.T. Lin, P. Shen, J. Solid State Chem. 145 (1999) 739–750.
[4] M.L. Jeng, P. Shen, J. Solid State Chem. 152 (2000) 421–427.
[5] P. Shen, J.Y. Wang, J. Solid State Chem. 161 (2001) 341–347.
[6] T.R. Welberry, A.G. Christy, J. Solid State Chem. 117 (1995) 398–406.
[7] W.H. Lee, P. Shen, J. Solid State Chem. 177 (2004) 101–108.
[8] M.Y. Li, P. Shen, S.L. Hwang, Mater. Sci. Eng. A 343 (2003) 227–234.
[9] K.C. Yang, P. Shen, J. Solid State Chem. 178 (2005) 661–670.
[10] E.W. Cahn, Mater. Today 4 (2002) 13.
[11] A. Putnis, Introduction to Mineral Sciences, Cambridge University Press, Cambridge, 1992, pp. 1–457.
[12] S.L. Hwang, P. Shen, H.T. Chu, T.F. Yui, Science 288 (2000) 321–324.
[13] P. Shen, S.L. Hwang, H.T. Chu, T.F. Yui, Int Geol Rev 43 (2001) 366–378.
[14] V. Jayaram, Philos. Mag. A 57 (1988) 525–542.
[15] S.Q. Xiao, U. Dahmen, A.H. Heuer, Philos. Mag. A 75 (1997) 221–238.
[16] A.E. McHale, R.S. Roth, J. Am. Ceram. Soc. 69 (11) (1986) 827–832.
[17] T.R. Welberry, R.L. Withers, J.G. Thompson, B.D. Butler, J. Solid State Chem. 100 (1992) 71–89.
[18] T.R. Welberry, R.L. Withers, S.C. Mayo, J. Solid State Chem. 115 (1995) 43–54.
[19] J.F. Banfield, D.R. Veblen, Am. Mineral. 76 (1991) 113–127.
[20] F.H. Brown Jr., P. Duwez, J. Am. Ceram. Soc. 37 (3) (1954) 129–132.
[21] O.T. Sørensen, Nonstoichiometric Oxides, Academic Press, New York, 1981.
[22] P. Kofstad, J. Phys. Chem. Solids 23 (1962) 1579–1586.
[23] K.S. Forland, Acta Chem. Scand. 18 (1964) 1267–1275.
[24] F.A. Kröger, H.J. Vink, Solid State Phys. 3 (1956) 307–435.
[25] A.N. Cormack, C.M. Freeman, C.R.A. Catlow, R.L. Royle, Defect structures and energetics in nonstoichiometric rutile, in: C.R.A. Catlow, W.C. Mackrodt (Eds.), Advances in Ceramics, vol. 23, Nonstoichiometric Compounds, American Ceramic Society, Westerville, OH, 1987, pp. 283–291.
[26] P. Kofstad, A.Z. Hed, J. Am. Ceram. Soc. 50 (12) (1967) 681–682.
[27] D.M. Duffy, Philos. Mag. 50 (1984) 143–154.
[28] C. Gleitzer, F. Nowotny, M. Rekas, Appl. Phys. A 53 (1991) 310–316.
[29] J. Nowotny, I. Sikora, J.B. Wagner Jr., J. Am. Ceram. Soc. 65 (4) (1982) 192–196.
[30] R.D. Shannon, Acta Crystallogr. A 32 (1976) 751–767.
[31] A.G. Khachaturyan, Theory of Structural Transformations in Solids, Wiley, New York, 1983, pp. 534–541.
[32] A. Atkinson, Diffusion in oxides of the first transition-series metals, in: C.R.A. Catlow, W.C. Mackrodt (Eds.), Advances in Ceramics, vol. 23, Nonstoichiometric Compounds, Americane, Westerville, OH, 1987, pp. 3–26.
[33] B. Soffa, Diffusional pathways in the decomposition of alloys, International Conference on Solid-Solid Phase Transformation in Inorganic Materials, Phoenix, 2005.